Controllable Design of MoS$_2$ Nanosheets Anchored on Nitrogen-Doped Graphene: Toward Fast Sodium Storage by Tunable Pseudocapacitance

Xin Xu, Ruisheng Zhao, Wei Ai, Bo Chen, Hongfang Du, Lishu Wu, Hua Zhang, Wei Huang, and Ting Yu*

Transition-metal disulfide with its layered structure is regarded as a kind of promising host material for sodium insertion, and intensely investigated for sodium-ion batteries. In this work, a simple solvothermal method to synthesize a series of MoS$_2$ nanosheets@nitrogen-doped graphene composites is developed. This newly designed recipe of raw materials and solvents leads the success of tuning size, number of layers, and interplanar spacing of the as-prepared MoS$_2$ nanosheets. Under cut-off voltage and based on an intercalation mechanism, the ultrasmall MoS$_2$ nanosheets@nitrogen-doped graphene composite exhibits more preferable cycling and rate performance compared to few-/dozens-layered MoS$_2$ nanosheets@nitrogen-doped graphene, as well as many other reported insertion-type anode materials. Last, detailed kinetics analysis and density functional theory calculation are also employed to explain the Na$^+$-storage behavior, thus proving the significance in surface-controlled pseudocapacitance contribution at the high rate. Furthermore, this work offers some meaningful preparation and investigation experiences for designing electrode materials for commercial sodium-ion batteries with favorable performance.

Dr. X. Xu, Dr. W. Ai, Prof. W. Huang
Shaanxi Institute of Flexible Electronics (SIFE)
Northwestern Polytechnical University (NPU)
Xi'an 710129, China
E-mail: iamwhuang@nwpu.edu.cn
Dr. X. Xu, Dr. W. Ai, H. Du, L. Wu, Prof. T. Yu
Division of Physics and Applied Physics
School of Physical and Mathematical Sciences
Nanyang Technological University
Singapore 637371, Singapore
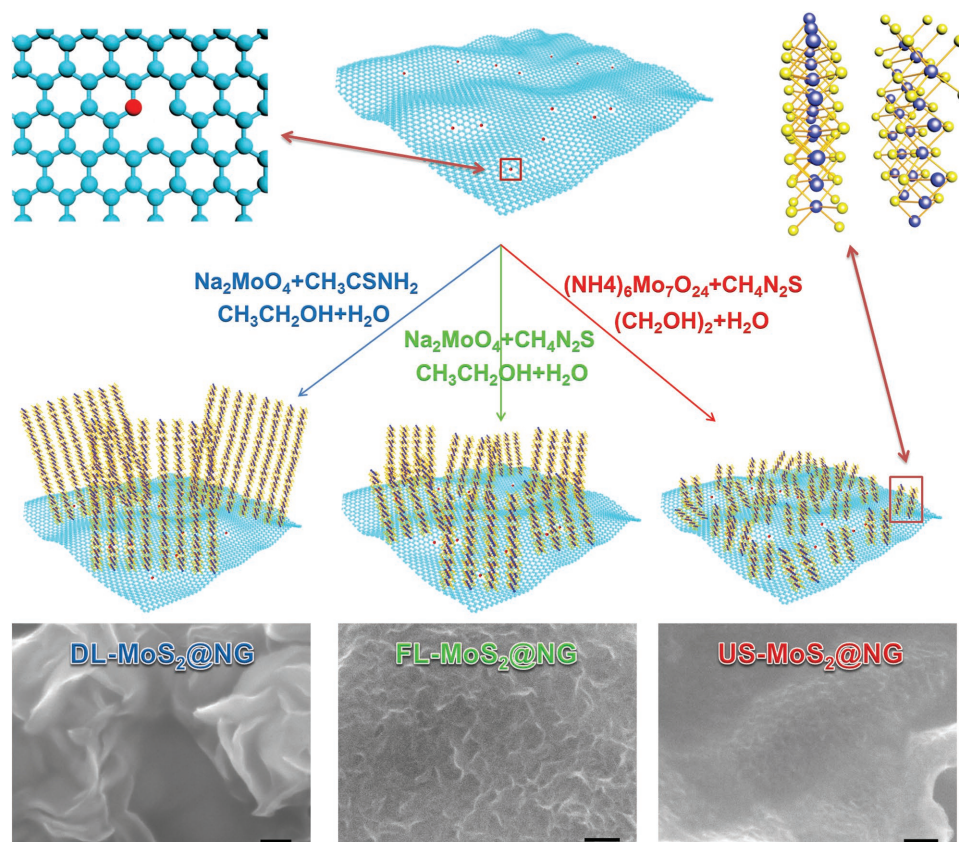E-mail: yuting@ntu.edu.sg
Dr. R. Zhao
Department of Applied Chemistry
School of Science
Xi'an Jiaotong University
Xi'an 710049, China
Dr. B. Chen, Prof. H. Zhang
School of Materials Science and Engineering
Nanyang Technological University
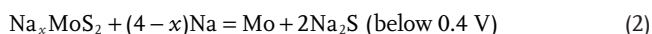Singapore 639798, Singapore
Prof. W. Huang
Key Laboratory of Flexible Electronics (KLOFE) & Institute of Advanced Materials (IAM)
Nanjing Tech University (NanjingTech)
Nanjing 211816, China

Lithium-ion batteries (LIBs) have been regarded as one of the most significant energy storage devices in the past decades, along with the rapidly increasing electronics market.[1,2] As a result, the cost and consumption of raw material (Li$_2$CO$_3$) for LIBs were drastically increased during the last ten years.[3] Own to its low price and element abundance, sodium gradually attracts the academic attention and becomes a promising substitute of lithium for next-generation commercial rechargeable batteries.[4] However, due to the large ionic radius of Na$^+$ (1.02 Å) compared to Li$^+$ (0.76 Å), fabricating a more beneficial anode material aims to better Na$^+$ insertion and extraction is a pivotal object for sodium-ion batteries (SIBs or NIBs).[5–8] Very recently, alloying and conversion-based anode materials (e.g., Sb, P, SnS$_2$, and FeS$_2$) have been regularly investigated as the anode materials for NIBs.[9–13] Unfortunately, the large volume variations and serious agglomeration of the negative electrodes during the sodiation/desodiation processes give rise to a fast capacity decay. Although preparing nano-sized active components together with the carbon assistant can relieve the above-mentioned defects to some extent, the reported results are hard to fulfill the commercial applications yet. On the other hand, a series of Na$_2$Ti$_3$O$_7$ and TiO$_2$ nanostructures with intercalation mechanism also have been fabricated and employed for long-cycle-life sodium storage, but the limited specific capacities are still unsatisfactory.[14–16] Thus, developing a novel strategy or searching for a new kind of electrode material for NIBs is still desirable.

Molybdenum disulfide (MoS$_2$), a typical 2D transition-metal disulfide with large distance between stacked layers, was frequently investigated in both the LIBs and NIBs fields.[5,6,17–19] When an MoS$_2$-based anode is evaluated in Na$^+$ half-cells, intercalation and conversion reactions take place in order under a discharge process. As demonstrated in Equations (1) and (2), Na ions first insert into the MoS$_2$ interlayers with the discharge voltage varying from 3 to 0.4 V, and then Na$_x$MoS$_2$ fully transforms to metallic Mo and Na$_2$S when the potential is below 0.4 V.[20–22]

Figure 1. Schematic illustration of the synthesis procedures and morphologies of the DL-MoS$_2$@NG, FL-MoS$_2$@NG, and US-MoS$_2$@NG (Scale bars, 100 nm).

$$MoS_2 + xNa = Na_xMoS_2 \quad \text{(above 0.4 V, } x < 2) \tag{1}$$

$$Na_xMoS_2 + (4 - x)Na = Mo + 2Na_2S \text{ (below 0.4 V)} \tag{2}$$

Several former works report that controlling charge/discharge voltage through a cut-off method to ensure an intercalation process is able to significantly improve the cycling stability.[20,23,24] However, abandon of the conversion reaction means a sacrifice of theoretical capacity as well as increasing the operation voltage. Therefore, the promotion of the specific capacity of insertion-type MoS$_2$ electrode becomes more urgent.

It is generally accepted that during the discharge step, solvated ions (Li$^+$ or Na$^+$) can be stored by most of anode materials via not only a diffusion-controlled process but also a Faradaic charge transfer existing at or near the surface/subsurface of electrode material, that is, the so-called surface-controlled process, meanwhile leading to an extra pseudocapacitance.[25,26] Very recently, some groups demonstrated that decreasing the size of nano-scale metal disulfides and expanding the distance of interlayer are able to generate a considerable capacitive contribution, thus, resulting in an apparent improvement of specific capacities and rate performance.[20,27–30] On the other hand, the electrochemical properties of pure MoS$_2$-based materials are often critically impeded by their poor electric conductivity. To solve this problem, assembling MoS$_2$ nanostructures with carbon nanotubes or graphene is proved to be an effective approach.[31–34] For example, Yu et al. fabricated ultrathin MoS$_2$ nanowall arrays anchored on carbon layer hybrids through an in situ hybridization method and then tested them under a cut-off voltage (0.4–3.0 V), which displayed an excellent reversible capacity of 120 mAh g^{-1} at a high rate of 10 A g^{-1}.[34]

In this work, a kind of hierarchical nitrogen-doped graphene (NG) sheets synthesized by our group is first employed as a conductive scaffold for growing active nanostructures (Figure S1, Supporting Information).[35] A simple solvothermal approach is introduced to construct a series of MoS$_2$ nanosheets (dozens layered MoS$_2$ nanosheets: DL-MoS$_2$; few layered MoS$_2$ nanosheets: FL-MoS$_2$; ultrasmall MoS$_2$ nanosheets: US-MoS$_2$) anchored on the NG to form the final hybrid anode materials (denoted as DL-MoS$_2$@NG, FL-MoS$_2$@NG, and US-MoS$_2$@NG). By rationally changing the raw sources and solvents, the as-obtained MoS$_2$ nanosheets exhibit tunable size and number of layers as well as interplanar spacing. The synthesis routes including the morphologies of the MoS$_2$ nanosheets are illustrated in **Figure 1**. From the scanning electron microscopic images, we can recognize that the three kinds of MoS$_2$ nanosheets reveal a "standing" feature and the lateral sizes are about 100–400, 50–100, and 10–50 nm, respectively. In addition, the low-resolution observations of the samples show that both sides of the NG sheets are uniformly covered with MoS$_2$ nanosheets, indicating the suitable in situ hybridization and self-assembly processes (Figure S2, Supporting information).[36–38] As the anode materials for NIBs, the US-MoS$_2$@NG exhibits the best electrochemical
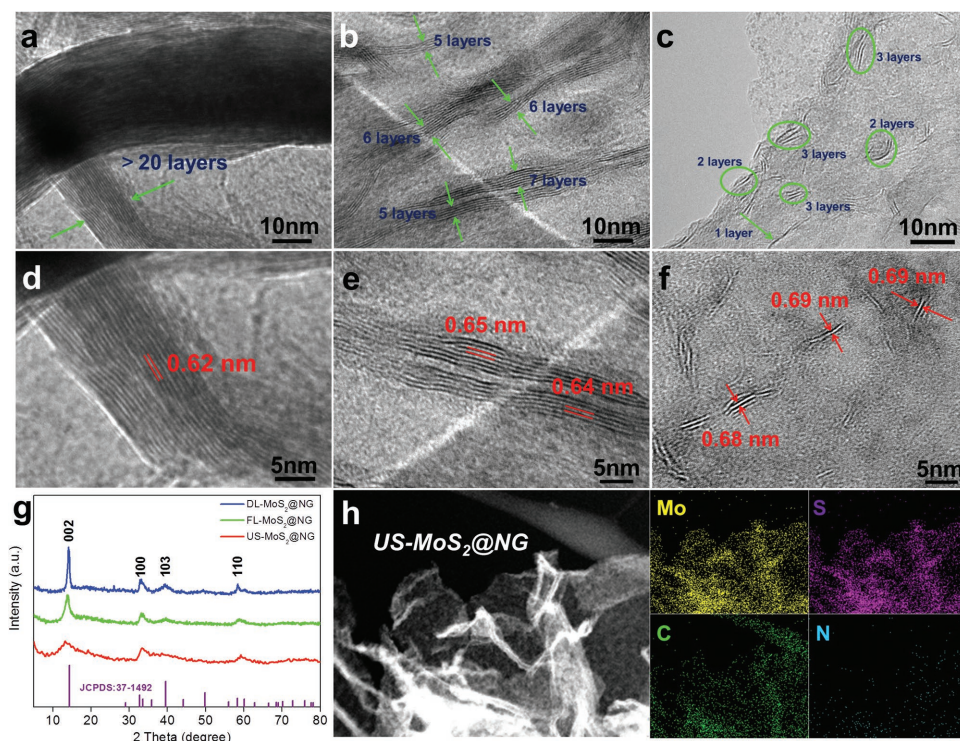
Figure 2. High-resolution transmission electron microscopy images of the DL-MoS$_2$@NG a,d), FL-MoS$_2$@NG b,e), and US-MoS$_2$@NG c,f), respectively. g) XRD patterns of the different MoS$_2$@NG samples. h) Transmission electron microscopic image and elemental mapping of US-MoS$_2$@NG.

behavior among the three candidates, which can be ascribed to the favorably designed MoS$_2$ nanosheets with more active S edges on the surface and expanded interlayer spacing for Na$^+$ storage.

Detailed structure and composition information of the three samples are shown in **Figure 2**. As can be seen, a thick MoS$_2$ nanosheet with dozens of atomic layers can be observed from the DL-MoS$_2$@NG composite (Figure 2a). By changing the sulfur source from thioacetamide to thiourea, the thickness of the as-prepared MoS$_2$ nanosheets decreases to about five to seven layers (Figure 2b). Figure 2c shows that with the assistant of ethylene glycol, the thickness of the as-obtained MoS$_2$ nanosheets is further reduced to one to three layers. Moreover, the interlayer distances of the three samples display a gradually increasing trend, which can be clearly noticed from Figure 2d–f. Based on the former results, expanded interlayers of MoS$_2$ could effectively increase the amount of Na$^+$ intercalation at a high rate.[20] This fact is also confirmed by the X-ray diffraction (XRD) examination in Figure 2g, the peaks of (002) plane for FL-MoS$_2$@NG and US-MoS$_2$@NG indicate a slight shift to the lower scattering angle compared with the DL-MoS$_2$@NG. Besides, all of the XRD peaks of the three samples can be distinctly identified and matched with the JCPDS card (No. 37–1492) of hexagonal 2H-MoS$_2$. Figure 2h displays the detailed element distribution for US-MoS$_2$@NG composites by scanning transmission electron microscopy, revealing a uniform hybridization of MoS$_2$ nanosheets and nitrogen-doped graphene again.

To determine the accurate elemental composition of the final products, we choose the US-MoS$_2$@NG as an instance

and investigate it by X-ray photoelectron spectroscopy (XPS), as shown in Figure S3 of the Supporting Information. From the survey spectrum, we can see that the US-MoS$_2$@NG is constituted by Mo, S, C, N, and O (Figure S3a, Supporting Information). In detail, two peaks located at 229.6 and 232.8 eV represent the Mo 3d$_{5/2}$ and Mo 3d$_{3/2}$, respectively, and suggest the presence of Mo^{4+} state in the composite (Figure S3b, Supporting Information). Two additional peaks at 162.5 and 163.6 eV related to S 2p$_{3/2}$ and S 2p$_{1/2}$ of S^{2-} can be clearly observed from Figure S3c of the Supporting Information. The C 1s spectrum (Figure S3d, Supporting Information) shows three peaks at 284.7 (C=C), 286.7 (C–N/C–O), and 288.9 eV (C=O). In Figure S3e of the Supporting Information, the three deconvoluted peaks located at about 398.4, 399.8, and 401.3 eV can be assigned to the pyridine-like N, pyrrole-like N, and graphite-like N, respectively.[35,39–41] Furthermore, the active material (MoS$_2$) contents of the samples are tested by thermogravimetric analysis, and the curves are revealed in Figure S4 of the Supporting Information. By presuming that the final substances are MoO$_3$ after calcination processes in oxygen atmosphere, the mass fraction of MoS$_2$ in the DL-MoS$_2$@NG, FL-MoS$_2$@NG, and US-MoS$_2$@NG are 95.6%, 93.6%, and 87.5%, respectively.[42] The specific surface areas of the different MoS$_2$@NG samples are also investigated by N$_2$ adsorption–desorption isotherms and the results are shown in Figure S5 of the Supporting Information. As calculated by Brunauer–Emmett–Teller method, the US-MoS$_2$@NG displays a higher specific area (49 m^2 g^{-1}) than that of FL-MoS$_2$@NG and DL-MoS$_2$@NG (19 and 4 m^2 g^{-1}), which is more beneficial for Na$^+$ storage.
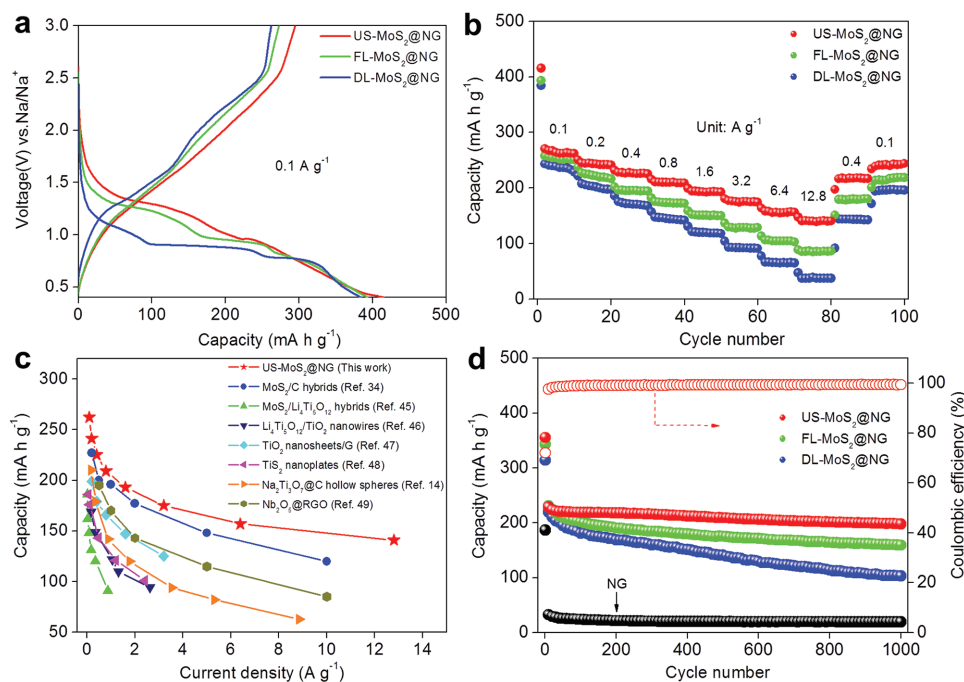
Figure 3. Na$^+$ storage performance of the different samples. a) The first charge–discharge voltage profiles at 0.1 A g^{-1} and b) rate capabilities of the three MoS$_2$@NG samples. c) A comparison of rate performance of US-MoS$_2$@NG with some other reported insertion-type anode materials. d) Cycling investigation of the as-prepared products at 1 A g^{-1}, including the corresponding Coulombic efficiency of US-MoS$_2$@NG.

Figure 3 presents the Na$^+$ intercalation behavior of the as-prepared anode materials under a cut-off voltage (0.4–3 V), including both the rate and cycling performance. In detail, Figure 3a displays the voltage profiles of the three MoS$_2$@NG samples during the first charge–discharge cycle at 0.1 A g^{-1}. The discharge-specific capacities of the US-MoS$_2$@NG, FL-MoS$_2$@NG, and DL-MoS$_2$@NG anodes are 416, 393, and 384 mAh g^{-1}, respectively. More importantly, the US-MoS$_2$@NG shows the highest potential of the discharge platform, which can be attributed to the largest lattice distance between the MoS$_2$ layers and, thus, resulting in the lowest barrier energy of Na$^+$ intercalation.[20,43,44] This phenomenon is also confirmed by their CV results, which are presented in Figure S6a–c of the Supporting Information. Figure 3b shows the rate performance of the three samples. As can be seen, the US-MoS$_2$@NG anode reveals a reversible capacity of 141 mAh g^{-1} even under a high rate of 12.8 A g^{-1}, which is more favorable than that of FL-MoS$_2$@NG and DL-MoS$_2$@NG (86 and 38 mAh g^{-1}). In addition, it can be obviously discovered that the capacity differences of the three samples are increased in order with the rising of the current densities, which means more beneficial intercalation reaction kinetics possessed by US-MoS$_2$@NG. Moreover, the US-MoS$_2$@NG composite still displays similar rate performance even under higher mass loading (>2.0 mg cm^{-2}; Figure S7, Supporting information). To best of our knowledge, the rate capability of the US-MoS$_2$@NG is superior to that of many other insertion-type electrode materials previously reported, such as the MoS$_2$/C hybrids,[34] MoS$_2$/Li$_4$Ti$_5$O$_{12}$ hybrids,[45] Li$_4$Ti$_5$O$_{12}$/TiO$_2$ nanowire arrays,[46] TiO$_2$ nanosheets/graphene composites,[47] TiS$_2$ nanoplates,[48] Na$_2$Ti$_3$O$_7$@C hollow spheres,[14] and Nb$_2$O$_5$@RGO composites[49] for NIBs (Figure 3c).

This more favorable sodium-storage behavior demonstrated by US-MoS$_2$@NG can be ascribed to its reasonable structural design, which will be discussed later in detail. The cycling tests are also employed to further evaluate the sodium-storage performance of the as-prepared products. Figure S8 of the Supporting Information shows the 1st, 10th, and 50th charge/discharge voltage curves of US-MoS$_2$@NG anode at 1 A g^{-1}, which reveals an excellent reversible capability of the charge and discharge capacities except for the first cycle. From Figure 3d, we can see that the US-MoS$_2$@NG is robust enough to achieve a highly stable cycling performance, illustrating a specific capacity of 198 mAh g^{-1} at 1 A g^{-1} after 1000 cycles, leading an average reversible capacity loss of 0.03 mAh g^{-1} per cycle. As shown in Figure S9 of the Supporting Information, the US-MoS$_2$@NG composite can still retain its hierarchical morphology after cycling performance, thus proving the favorable structural stability during the electrochemical reactions. As a contrast, the cycling stability of the FL-MoS$_2$@NG and DL-MoS$_2$@NG is more inferior. In addition, the discharge capacities of the NG are around 20 mAh g^{-1} at the same current density, suggesting that the main capacities of the MoS$_2$@NG composites are contributed by the extrinsic MoS$_2$ shell. The different MoS$_2$@NG anodes are also tested at relatively low current densities (200 mA g^{-1}), with final discharge capacities of 238, 213, and 174 mAh g^{-1} after 400 cycles, respectively (Figure S10, Supporting Information). In addition, all of the MoS$_2$@NG samples are investigated by Nyquist plots, the US-MoS$_2$@NG exhibits the smallest semicircle diameter among the three kinds of MoS$_2$@NG composites, apparently indicating the lowest resistance (Figure S11, Supporting Information). To further explore whether the copper foil is involved in the

ADVANCED
SCIENCE NEWS
www.advancedsciencenews.com

ADVANCED
MATERIALS
www.advmat.de
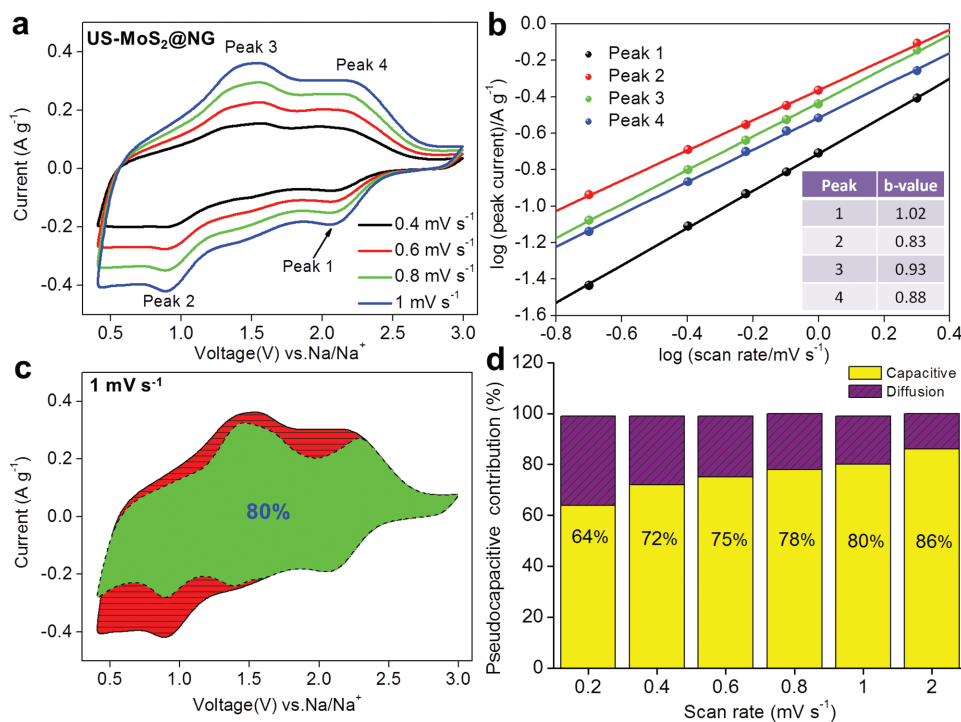
Figure 4. Kinetics and quantitative analysis of the Na⁺ storage behavior of US-MoS₂@NG anode. a) CV curves at different scan rate. b) Logarithm peak current versus logarithm scan rate plots (inset: a summary of the calculated *b* values). c) Separation of capacitive (green region) and diffusion-controlled (red region) contribution at 1 mV s⁻¹. d) The percentages of pseudocapacitive contribution at different scan rates.

electrochemical reactions, we apply the EDS element mapping test to the cycled US-MoS₂@NG electrode. As shown in Figure S12 in the Supporting Information, all of the related elements except for the Cu can be discovered clearly, thus confirming that the main capacities are contributed by MoS₂@NG composites. When a Ti foil is used as a current collector, the US-MoS₂@NG can still maintain its stable cycling performance (Figure S13, Supporting Information).

To further investigate the relationship between the pseudocapacitance-like contribution and rate performance of the as-prepared MoS₂@NG samples, we employ the kinetics and quantitative analysis by a series of CV measurements immediately. **Figure 4**a shows the stepwise CV curves of US-MoS₂@NG electrode under the scan rates ranging from 0.4 to 1 mV s⁻¹. As can be seen, all of the CV curves display analogous shapes with four redox peaks distributed in the reduction and oxidation processes, indicating an obvious pseudocapacitive behavior. Moreover, when the scan rates increased to 2–10 mV s⁻¹, the redox peaks can still retain (Figure S6d, Supporting Information). It is well known that the current (i) and scan rate (v) of a CV curve are dominated by the equation: $I = av^b$, and the value of b relies on the solvated ions storage mechanism ($b = 0.5$, extreme diffusion-controlled process; $b = 1$, extreme pseudocapacitive-controlled process).[2,25,26] In Figure 4b, the logarithm peak currents against logarithm scan rates with linear relation are drawn for next calculations, thus the b values of the four redox peaks can be acquired as 1.02, 0.83, 0.93, and 0.88, respectively. This fact suggests that a mixed process existed in the US-MoS₂@NG anode, but the surface-controlled capacitive Na⁺ storage mechanism should be more dominant (compared to

the b values of FL-MoS₂@NG and DL-MoS₂@NG; Figure S14b and S15b, Supporting Information). To be more accurate, the quantitative capacitive contribution under the given scan rate can be obtained from another equation: $i = k_1v + k_2v^{1/2}$, where k_1 and k_2 represent the surface pseudocapacitive-controlled and diffusion-controlled processes, respectively. For example, Figure 4c illustrates a separation of pseudocapacitive-controlled current from the entire CV curve at 1 mV s⁻¹. The capacitive contribution of US-MoS₂@NG is around 80% and higher than that of FL-MoS₂@NG (≈73%; Figure S14c, Supporting Information) and DL-MoS₂@NG (≈66%; Figure S15c, Supporting Information), which determines a more favorable sodium-storage behavior under high current densities. Figure 4d shows that the pseudocapacitive contribution percentages are raised in order with the increasing of the scan rates.

The above results show that the surface-controlled capacitive contribution is more meaningful than that of diffusion-controlled process at high rate, which can also be further explained by the energy barriers of Na⁺ storage through these two approaches. Based on first principle, the diffusion of Na⁺ is simulated by density functional theory (DFT) methods. **Figure 5**a demonstrates the top-view structure of MoS₂ layer. In order to simplify the calculation, we considered two models of single and double MoS₂ layer(s) (Figure 5b,c). After lattice relaxation, the lattice parameters for the two models are $a = b = 8.451$ Å and $a = b = 8.457$ Å, respectively. As for the former model, Na ions diffuse on the surface of MoS₂ layer. For the latter one, Na ions diffuse in the interspace between two MoS₂ layers, and the diffusion path is from the site on the top of Mo to S. The energy barriers of Na⁺ diffusion in single MoS₂ layer
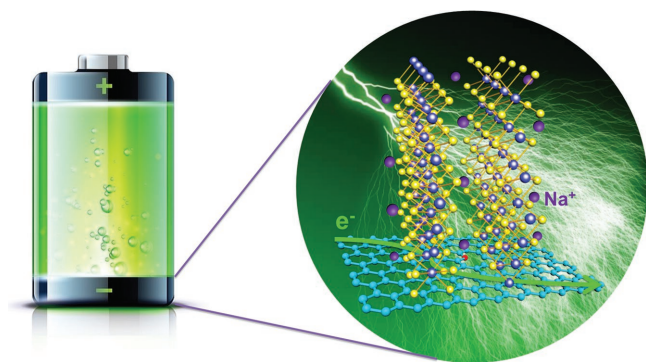
ADVANCED
SCIENCE NEWS
www.advancedsciencenews.com

ADVANCED
MATERIALS
www.advmat.de
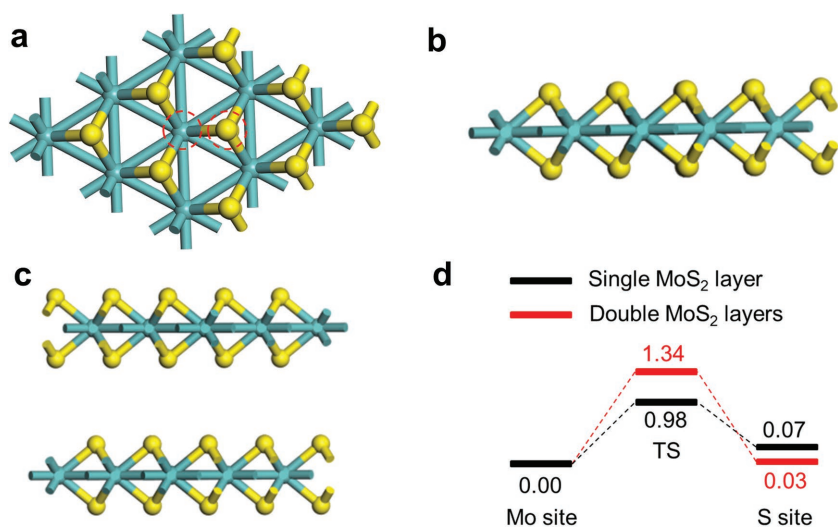
Figure 5. a) Top-view structure of MoS$_2$ layer. b) Side-view of single MoS$_2$ layer. c) Side-view of double MoS$_2$ layers. d) Energy profile (in eV) of Na$^+$ diffusion. (S: yellow, Mo: green).

solvothermal methods. Under a cut-off voltage and based on a intercalation mechanism, the US-MoS$_2$@NG anode displays the most favorable Na$^+$ storage properties including both the rate and cycling performance. By means of the kinetics and quantitative analysis, a surface-dominated Na$^+$ storage process is obviously improved by the rational design of the MoS$_2$ nanosheets, thus providing a conclusive evidence of the considerable charge storage at high rate. In addition, the more accessible Na$^+$ diffusion and storage on the surface compared to interlayers of MoS$_2$ are further confirmed by the DFT calculations. In one word, the findings and completions achieved in this work are promising for developing electordes with high sodium-storage performance toward next-generation energy-related applications.

and double MoS$_2$ layers are calculated to be 0.98 and 1.34 eV, respectively, indicating that Na ions diffuse more readily on the MoS$_2$ surface compared to the interspace between MoS$_2$ layers.

The experimental and calculation results present that the US-MoS$_2$@NG composite possesses a superior sodium-storage capability among the three MoS$_2$@NG samples as well as compared to many other insertion-type anode materials. As illustrated in **Figure 6**, the enhanced electrochemical behavior of US-MoS$_2$@NG can be ascribed to four points: (i) the ultrathin MoS$_2$ nanosheets can effectively shorten the transport path and lower the energy barriers of Na$^+$ diffusion; (ii) MoS$_2$ nanosheets with decreased size is capable of providing more active sites for Na$^+$ adsorption and reaction; (iii) the expanded interlayers of MoS$_2$ are able to reduce the resistance of charge transfer, thus improving the intercalation/extraction of Na$^+$ during the discharge/charge processes; (iv) the hierarchical N-doped graphene can not only strengthen the structure stability but also increase the electrical conductivity of the whole composites.

In conclusion, a series of MoS$_2$ nanosheets with tunable size, number of layers, and interlayer distances are constructed on the hierarchical N-doped graphene sheets through simple

Supporting Information

Acknowledgements

Conflict of Interest

The authors declare no conflict of interest.

Keywords

Figure 6. Schematic illustration of the Na$^+$ storage and electron transportation in the US-MoS$_2$@NG anode.

[1] M. Armand, J. M. Tarascon, *Nature* **2008**, *451*, 652.
[2] P. Simon, Y. Gogotsi, B. Dunn, *Science* **2014**, *343*, 1210.
[3] N. Yabuuchi, K. Kubota, M. Dahbi, S. Komaba, *Chem. Rev.* **2014**, *114*, 11636.

[4] W. Luo, F. Shen, C. Bommier, H. Zhu, X. Ji, L. Hu, *Acc. Chem. Res.* **2016**, *49*, 231.

[5] J. Sun, H. W. Lee, M. Pasta, H. Yuan, G. Zheng, Y. Sun, Y. Li, Y. Cui, *Nat. Nanotechnol.* **2015**, *10*, 980.

[6] X. Xie, T. Makaryan, M. Zhao, K. L. V. Aken, Y. Gogotsi, G. Wang, *Adv. Energy Mater.* **2016**, *6*, 1502161.

[7] X. Wang, C. Niu, J. Meng, P. Hu, X. Xu, X. Wei, L. Zhou, K. Zhao, W. Luo, M. Yan, L. Mai, *Adv. Energy Mater.* **2015**, *5*, 1500716.

[8] D. Guan, Q. Yu, C. Xu, C. Tang, L. Zhou, D. Zhao, L. Mai, *Nano Res.* **2017**, *10*, 4351.

[9] Z. Liu, X. Y. Yu, X. W. Lou, U. Paik, *Energy Environ. Sci.* **2016**, *9*, 2314.

[10] J. Liu, L. Yu, C. Wu, Y. Wen, K. Yin, F. K. Chiang, R. Hu, J. Liu, L. Sun, L. Gu, J. Maier, Y. Yu, M. Zhu, *Nano Lett.* **2017**, *17*, 2034.

[11] J. Qian, X. Wu, Y. Cao, X. Ai, H. Yang, *Angew. Chem., Int. Ed.* **2013**, *52*, 4731.

[12] Y. Jiang, M. Wei, J. Feng, Y. Ma, S. Xiong, *Energy Environ. Sci.* **2016**, *9*, 1430.

[13] Z. Liu, T. Lu, T. Song, X. Y. Yu, X. W. Lou, U. Paik, *Energy Environ. Sci.* **2017**, *10*, 1576.

[14] F. Xie, L. Zhang, D. Su, M. Jaroniec, S. Z. Qiao, *Adv. Mater.* **2017**, *29*, 1700989.

[15] C. Chen, Y. Wen, X. Hu, X. Ji, M. Yan, L. Mai, P. Hu, B. Shan, Y. Huang, *Nat. Commun.* **2014**, *6*, 6929.

[16] Y. Zhang, Z. Ding, C. W. Foster, C. E. Banks, X. Qiu, X. Ji, *Adv. Funct. Mater.* **2017**, *27*, 1700856.

[17] S. Wang, B. Y. Guan, L. Yu, X. W. Lou, *Adv. Mater.* **2017**, *29*, 1702724.

[18] X. Cao, C. Tan, X. Zhang, W. Zhao, H. Zhang, *Adv. Mater.* **2016**, *28*, 6167.

[19] Y. Liu, X. He, D. Hanlon, A. Harvey, J. N. Coleman, Y. Li, *ACS Nano* **2016**, *10*, 8821.

[20] Z. Hu, L. Wang, K. Zhang, J. Wang, F. Cheng, Z. Tao, J. Chen, *Angew. Chem., Int. Ed.* **2014**, *53*, 12794.

[21] Y. X. Wang, S. L. Chou, D. Wexler, H. K. Liu, S. X. Dou, *Chem. Eur. J.* **2014**, *20*, 9607.

[22] Q. Li, Z. Yao, J. Wu, S. Mitra, S. Hao, T. S. Sahu, Y. Li, C. Wolverton, V. P. Dravid, *Nano Energy* **2017**, *38*, 342.

[23] K. Zhang, Z. Hu, X. Liu, Z. Tao, J. Chen, *Adv. Mater.* **2015**, *27*, 3305.

[24] Z. Hu, Z. Zhu, F. Cheng, K. Zhang, J. Wang, C. Chen, J. Chen, *Energy Environ. Sci.* **2015**, *8*, 1309.

[25] H. S. Kim, J. B. Cook, H. Lin, J. S. Ko, S. H. Tolbert, V. Ozolins, B. Dunn, *Nat. Mater.* **2017**, *16*, 454.

[26] L. Wang, Y. Dong, K. Zhao, W. Luo, S. Li, L. Zhou, L. Mai, *Phys. Chem. Chem. Phys.* **2017**, *19*, 13341.

[27] D. Chao, C. Zhu, P. Yang, X. Xia, J. Liu, J. Wang, X. Fan, S. V. Savilov, J. Lin, H. J. Fan, Z. X. Shen, *Nat. Commun.* **2016**, *7*, 12122.

[28] J. B. Cook, H. S. Kim, T. C. Lin, C. H. Lai, B. Dunn, S. H. Tolbert, *Adv. Energy Mater.* **2017**, *7*, 1601283.

[29] G. A. Muller, J. B. Cook, H. S. Kim, S. H. Tolbert, B. Dunn, *Nano Lett.* **2015**, *15*, 1911.

[30] R. Sun, Q. Wei, J. Sheng, C. Shi, Q. An, S. Liu, L. Mai, *Nano Energy* **2017**, *35*, 396.

[31] X. Wang, G. Li, M. H. Seo, F. M. Hassan, M. A. Hoque, Z. Chen, *Adv. Energy Mater.* **2015**, *5*, 1501106.

[32] X. Xu, D. Yu, H. Zhou, L. Zhang, C. Xiao, C. Guo, S. Guo, S. Ding, *J. Mater. Chem. A* **2016**, *4*, 4375.

[33] X. Xie, T. Makaryan, M. Zhao, K. L. V. Aken, Y. Gogotsi, G. Wang, *Adv. Energy Mater.* **2016**, *6*, 1502161.

[34] Y. L. Ding, P. Kopold, K. Hahn, P. A. Aken, J. Maier, Y. Yu, *Adv. Mater.* **2016**, *28*, 7774.

[35] W. Ai, J. Jiang, J. Zhu, Z. Fan, Y. Wang, H. Zhang, W. Huang, T. Yu, *Adv. Energy Mater.* **2015**, *5*, 1500559.

[36] X. Xu, Z. Fan, S. Ding, D. Yu, Y. Du, *Nanoscale* **2014**, *6*, 5245.

[37] Y. Luo, D. Kong, J. Luo, S. Chen, D. Zhang, K. Qiu, X. Qi, H. Zhang, C. M. Li, T. Yu, *RSC Adv.* **2013**, *3*, 14413.

[38] X. Xu, Z. Fan, X. Yu, S. Ding, D. Yu, X. W. Lou, *Adv. Energy Mater.* **2014**, *4*, 1400902.

[39] X. Zhang, R. Zhao, Q. Wu, W. Li, C. Shen, L. Ni, H. Yan, G. Diao, M. Chen, *ACS Nano* **2017**, *11*, 8429.

[40] W. Ai, W. Zhou, Z. Du, Y. Du, H. Zhang, X. Jia, L. Xie, M. Yi, T. Yu, W. Huang, *J. Mater. Chem.* **2012**, *22*, 23439.

[41] Y. Luo, D. Kong, Y. Jia, J. Luo, Y. Lu, D. Zhang, K. Qiu, C. M. Li, T. Yu, *RSC Adv.* **2013**, *3*, 5851.

[42] L. Zhang, X. W. Lou, *Chem. Eur. J.* **2014**, *20*, 5219.

[43] J. Xiao, X. J. Wang, X. Q. Yang, S. D. Xun, G. Liu, P. K. Koech, J. Liu, J. P. Lemmon, *Adv. Funct. Mater.* **2011**, *21*, 2840.

[44] G. D. Du, Z. P. Guo, S. Q. Wang, R. Zeng, Z. X. Chen, H. K. Liu, *Chem. Commun.* **2010**, *46*, 1106.

[45] G. Xu, L. Yang, X. Wei, J. Ding, J. Zhong, P. K. Chu, *Adv. Funct. Mater.* **2016**, *26*, 3349.

[46] L. Gao, L. Wang, S. Dai, M. Cao, Z. Zhong, Y. Shen, M. Wang, *J. Power Sources* **2017**, *344*, 223.

[47] A. Shoaib, Y. Huang, J. Liu, J. Liu, M. Xu, Z. Wang, R. Chen, J. Zhang, F. Wu, *J. Power Sources* **2017**, *342*, 405.

[48] Y. Liu, H. Wang, L. Cheng, N. Han, F. Zhao, P. Li, C. Jin, Y. Li, *Nano Energy* **2016**, *20*, 168.

[49] L. Yan, G. Chen, S. Sarker, S. Richins, H. Wang, W. Xu, X. Rui, H. Luo, *ACS Appl. Mater. Interfaces* **2016**, *8*, 22213.